High-order fractal states in graphene superlattices

R. Krishna Kumar[a,b], A. Mishchenko[a,b], X. Chen[b], S. Pezzini[c], G. H. Auton[b], L. A. Ponomarenko[d], U. Zeitler[c], L. Eaves[a,e], V. I. Fal'ko[a,b,1], and A. K. Geim[a,b,1]

[a]School of Physics & Astronomy, University of Manchester, M13 9PL Manchester, United Kingdom; [b]National Graphene Institute, University of Manchester, M13 9PL Manchester, United Kingdom; [c]High Field Magnet Laboratory, Radboud University, 6525 ED Nijmegen, The Netherlands; [d]Department of Physics, University of Lancaster, LA1 4YW Lancaster, United Kingdom; and [e]School of Physics and Astronomy, University of Nottingham, NG7 2RD Nottingham, United Kingdom

Contributed by A. K. Geim, April 11, 2018 (sent for review March 16, 2018; reviewed by Allan H. MacDonald and Barbaros Oezyilmaz)

Graphene superlattices were shown to exhibit high-temperature quantum oscillations due to periodic emergence of delocalized Bloch states in high magnetic fields such that unit fractions of the flux quantum pierce a superlattice unit cell. Under these conditions, semiclassical electron trajectories become straight again, similar to the case of zero magnetic field. Here, we report magnetotransport measurements that reveal second-, third-, and fourth-order magnetic Bloch states at high electron densities and temperatures above 100 K. The recurrence of these states creates a fractal pattern intimately related to the origin of Hofstadter butterflies. The hierarchy of the fractal states is determined by the width of magnetic minibands, in qualitative agreement with our band-structure calculations.

graphene | superlattice | Hofstadter butterfly

For electrons in solids, their ability to freely propagate through the crystal lattice (Fig. 1*A*) originates from the translational invariance of the Hamiltonian associated with a periodic lattice potential. According to Bloch's theorem (1), the electronic states are dispersed in energy and described by wave functions that are delocalized over the entire crystal lattice. This description generally breaks down in the presence of magnetic field (B), because electrons experience the Lorentz force and become localized on closed orbits (2–5) (Fig. 1*B*). However, for certain B where the magnetic length is commensurable with the lattice periodicity (Fig. 1*C*), electrons recover delocalized wave functions (6, 7) and behave as "magnetic" Bloch states that propagate along open trajectories as if they are effectively in zero magnetic field ($B_{\rm eff} = 0$). Mathematically, this occurs for all rational fractions of magnetic flux $\phi = SB = \phi_0 p/q$, where S is the area of crystal's unit cell, ϕ_0 is the flux quantum, and p and q are integer numbers (6, 7). Physically, this is a consequence of the Aharonov–Bohm effect so that an electron passing across q unit cells acquires a phase shift in multiples of 2π, which restores the translational periodicity in high B. The recurrence of propagating Bloch states is expected to cause fractal, self-similar behavior in the magnetotransport properties of crystalline solids (6–8).

In graphene/hexagonal boron-nitride (hBN) superlattices (9–12), the periodic structure created by recurrent magnetic Bloch states was previously observed in low-temperature experiments (13–18), with most of the attention being paid to the detection of Landau gaps in the Hofstadter butterfly spectrum (8, 19). In particular, third-generation Dirac points (13), the anomalous quantum Hall effect (14), and replica quantum Hall ferromagnetism (16) were observed in the magnetic Bloch states that resided at unit fractions of $\phi/\phi_0 = 1/q$. However, this periodicity does not constitute the complete self-similarity inherent to magnetic Bloch states (6, 7) and Hofstadter butterflies (8, 19), where the spectra should replicate themselves at increasingly smaller scales of B. This fractal structure can appear only due to high-order magnetic Bloch states with numerator $p > 1$ and has awaited experimental confirmation.

In this article, we probe the electronic spectrum of graphene/hBN superlattices and report the full hierarchy of magnetic Bloch states up to the fourth order ($\phi/\phi_0 = 1/q$, $2/q$, $3/q$, and $4/q$) using an alternative approach that is based on the use of transport measurements at high temperatures (T = 100–200 K). In this regime, magnetotransport still reflects the characteristic properties of magnetic minibands but is not obscured by overlaying Shubnikov–de Haas (SdH) oscillations (20). Our recent work (21) showed that magnetic Bloch states become most prominent above 100 K, resulting in robust quantum oscillations in magnetoconductivity (σ_{xx}). These so-called Brown–Zak (BZ) oscillations originate from the repetitive formation of Bloch states at magnetic fields which follow the sequence $\phi/\phi_0 = 1/q$. Upon increasing B, electron trajectories are modulated between closed and open orbits, which cause the conductivity to oscillate. In the experiments below, we extend the parameter space to high carrier densities (n) and B up to 30 T, which allows the observation of a fractal pattern in σ_{xx} originating from high-order magnetic Bloch states ($p > 1$).

The studied devices were fabricated using the standard approach for making encapsulated graphene/hBN heterostructures (22) (for details, see *SI Appendix*, S1). During their assembly, a rotating stage was employed to accurately align graphene's crystallographic axes with the hBN substrate. The alignment resulted in a moiré superlattice (9–11, 23) with a period of ∼14 nm due to a slight (∼1.8%) mismatch between the graphene and hBN crystal lattices. This step is crucial to observe the physics described above, as it ensures that the regime with $\phi/\phi_0 = 1$ can be reached for B below 30 T. Note that for pristine graphene (without a superlattice potential) the above condition would be met only at ∼10,000 T. A second hBN crystal was placed on top of the graphene to encapsulate it, ensuring high electronic quality (24). The top hBN was intentionally misaligned to avoid a competing moiré potential acting on graphene

Significance

Electronic spectra of crystals in ultrahigh magnetic fields are expected to be fractal as symbolized by the theoretical plots called Hofstadter butterflies. Despite decades-long interest, their origin is often misconstrued. In fact, the fractal spectra can be understood as recurrence of delocalized Bloch states that appear each time the magnetic length becomes commensurate with the lattice periodicity. In this case, new quasiparticles emerge, moving through the crystal as if no magnetic field is applied. Their Landau quantization in noncommensurate fields generates the whole intricacy of Hofstadter spectra. Here, we study electron transport in graphene superlattices and report numerous self-similar features in their conductivity. This is a direct observation of the complete fractal pattern that underpins Hofstadter butterflies.

Author contributions: R.K.K., L.A.P., V.I.F., and A.K.G. designed research; R.K.K., A.M., X.C., S.P., G.H.A., U.Z., and A.K.G. performed research; R.K.K., A.M., X.C., L.A.P., V.I.F., and A.K.G. analyzed data; and R.K.K., L.E., V.I.F., and A.K.G. wrote the paper.

Reviewers: A.H.M., The University of Texas at Austin; and B.O., National University of Singapore.

The authors declare no conflict of interest.

[1]To whom correspondence should be addressed. Email: geim@manchester.ac.uk or vladimir.falko@manchester.ac.uk.

This article contains supporting information online at www.pnas.org/lookup/suppl/doi:10.1073/pnas.1804572115/-/DCSupplemental.

Published online April 30, 2018.

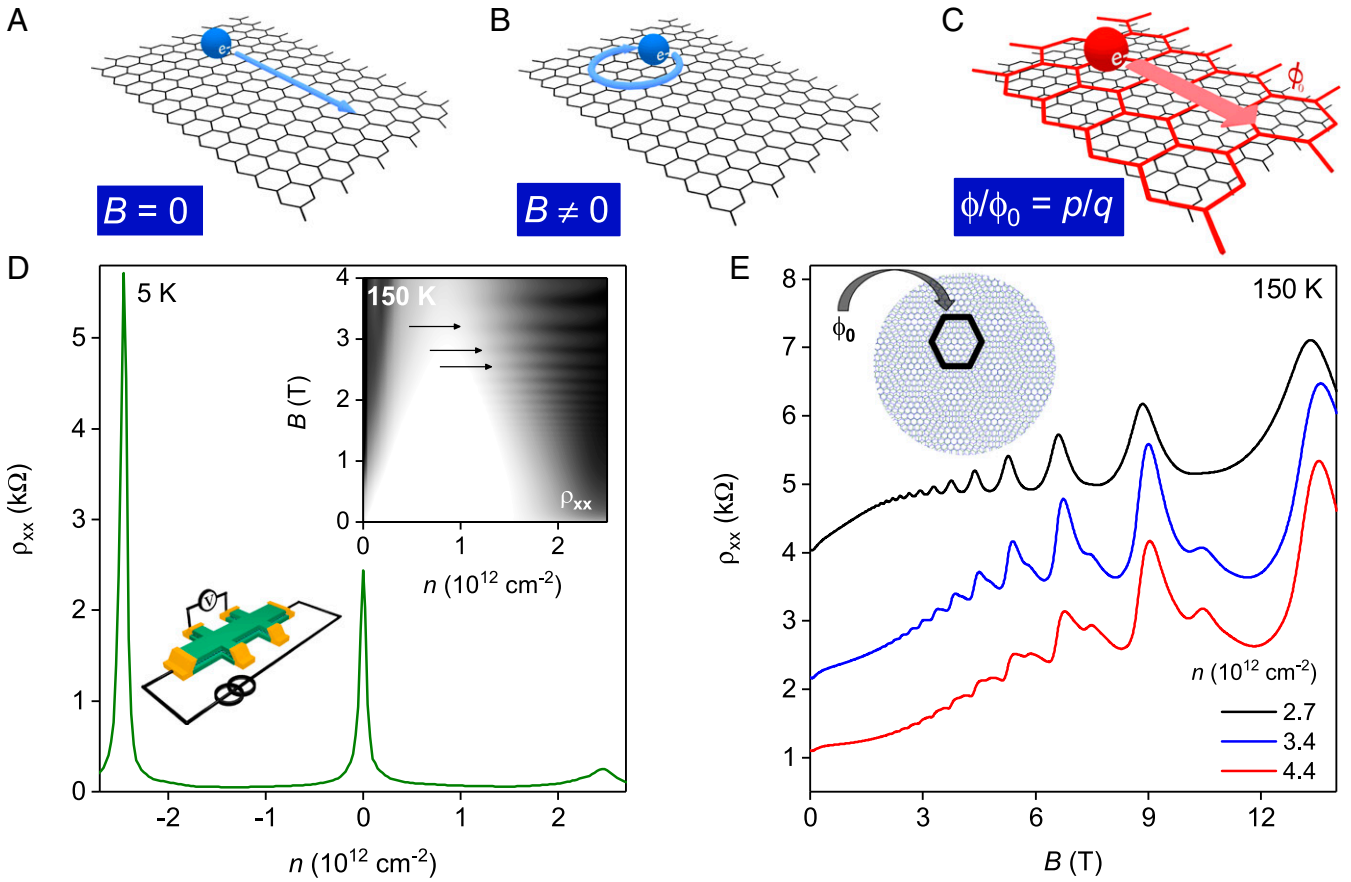

Fig. 1. BZ oscillations in graphene/hBN superlattices. (*A*–*C*) Schematic illustration of electron trajectories for different magnetic fields. The blue spheres (*A* and *B*) are electrons propagating along trajectories indicated in blue. Graphene's crystal lattice is shown as gray hexagons. The red sphere (*C*) represents a quasiparticle (magnetic Bloch state) propagating along a straight trajectory on a lattice of supercells (red hexagons), as if in zero effective magnetic field. Note however that in the presence of an electric field, trajectories in *C* may become curved and develop into chiral edge states because of nontrivial topology of the magnetic minibands (33–35, 39). (*D*) $\rho_{xx}(n)$ for a graphene superlattice with the period of ∼14 nm. (*Inset*) Map $\rho_{xx}(n,B)$ for electron doping. Logarithmic gray scale: white 80 Ω; black 1,200 Ω. (*Lower Inset*) Device and measurement schematics. (*E*) ρ_{xx} (*B*) at 150 K for three carrier densities above n_0. (*Inset*) Illustration of a graphene/hBN moiré superlattice. For $n = 2.7 \times 10^{12}$ cm^{-2}, the oscillations exhibit a single periodicity, which corresponds to one ϕ_0 piercing the moiré unit cell (outlined by the black hexagon).

charge carriers. After the assembly, electron beam lithography and standard microfabrication processing were employed to etch the heterostructure into multiterminal Hall bar devices with quasi–one-dimensional contacts (25, 26) (Fig. 1*D*, *Inset*). We studied five superlattice devices and found the features described below in all of them but they were strongest in those with the highest electronic quality and largest moiré period.

Fig. 1*D* shows an example of the measured resistivity (ρ_{xx}) in zero magnetic field as a function of n for one of our superlattice devices. Three peaks in ρ_{xx} are observed at $n = 0$ and $n = \pm 2.5 \times 10^{12}$ cm^{-2}. The latter two peaks provide an unambiguous indication of the superlattice reconstruction of graphene's spectrum (11, 27, 28) and are referred to as secondary Dirac points (DPs). Notably, the secondary DP is considerably sharper for hole doping (negative n) than electron doping (positive n), in agreement with the previous work (13–16) and with calculations that have demonstrated graphene's band structure is stronger modified for holes (27). Rather surprisingly, BZ oscillations are found to be more pronounced for electrons in the conduction band (21), especially at high T. Fig. 1*D* (*Inset*) plots a map of magnetoresistance ρ_{xx} (n, B) for electron doping at 150 K. At this T, SdH oscillations and the corresponding Landau fans (13–16) are completely suppressed because of thermal smearing. Instead, we find a set of horizontal streaks across the map (highlighted by arrows), which signifies magnetooscillations that are independent of n. These are BZ oscillations.

Fig. 1*E* plots ρ_{xx} (B) for several n beyond the electron secondary DP. For $n = 2.7 \times 10^{12}$ cm^{-2} (black curve), we find that ρ_{xx} oscillates in $1/B$ with a single periodicity of ϕ_0/S (schematic of Fig. 1*E*). As we increase n further, the oscillations start developing some extra periodicity. In particular, we find additional features appearing between the maxima. As shown below, these oscillations originate from the formation of magnetic Bloch states at $\phi/\phi_0 = 2/q$. Because the extra features become stronger at higher n and higher B, whereas standard doping by electrostatic gating is limited to $\sim 5 \times 10^{12}$ cm^{-2}, we employed fields up to 30 T and, at the same time, used optically induced doping, a peculiar property of graphene/hBN heterostructures (29) (*SI Appendix*, S2). These techniques allowed us to reach n as high as $\sim 3n_0$ and perform measurement for $\phi/\phi_0 \geq 1$.

It is instructive to analyze the BZ oscillations in terms of longitudinal conductivity σ_{xx} (B) = $\rho_{xx}/(\rho_{xx}^2 + \rho_{xy}^2)$, where ρ_{xy} is the Hall resistivity. This is because σ_{xx} exhibits local maxima at those Bs where magnetic Bloch states emerge ($\phi/\phi_0 = p/q$) and quasiparticle trajectories in the superlattice potential become effectively straight again, mimicking transport at zero field (30–32) (Fig. 1*C*). In addition, the use of the dissipative conductivity σ_{xx} simplifies our analysis by avoiding a nondissipative (Hall) contribution caused by topological properties of the magnetic minibands that can have nonzero Chern numbers (33–36). Fig. 2*A* plots σ_{xx} as a function of ϕ_0/ϕ, which emphasizes the $1/B$ periodicity of BZ oscillations. Here, we find local maxima in σ_{xx} located

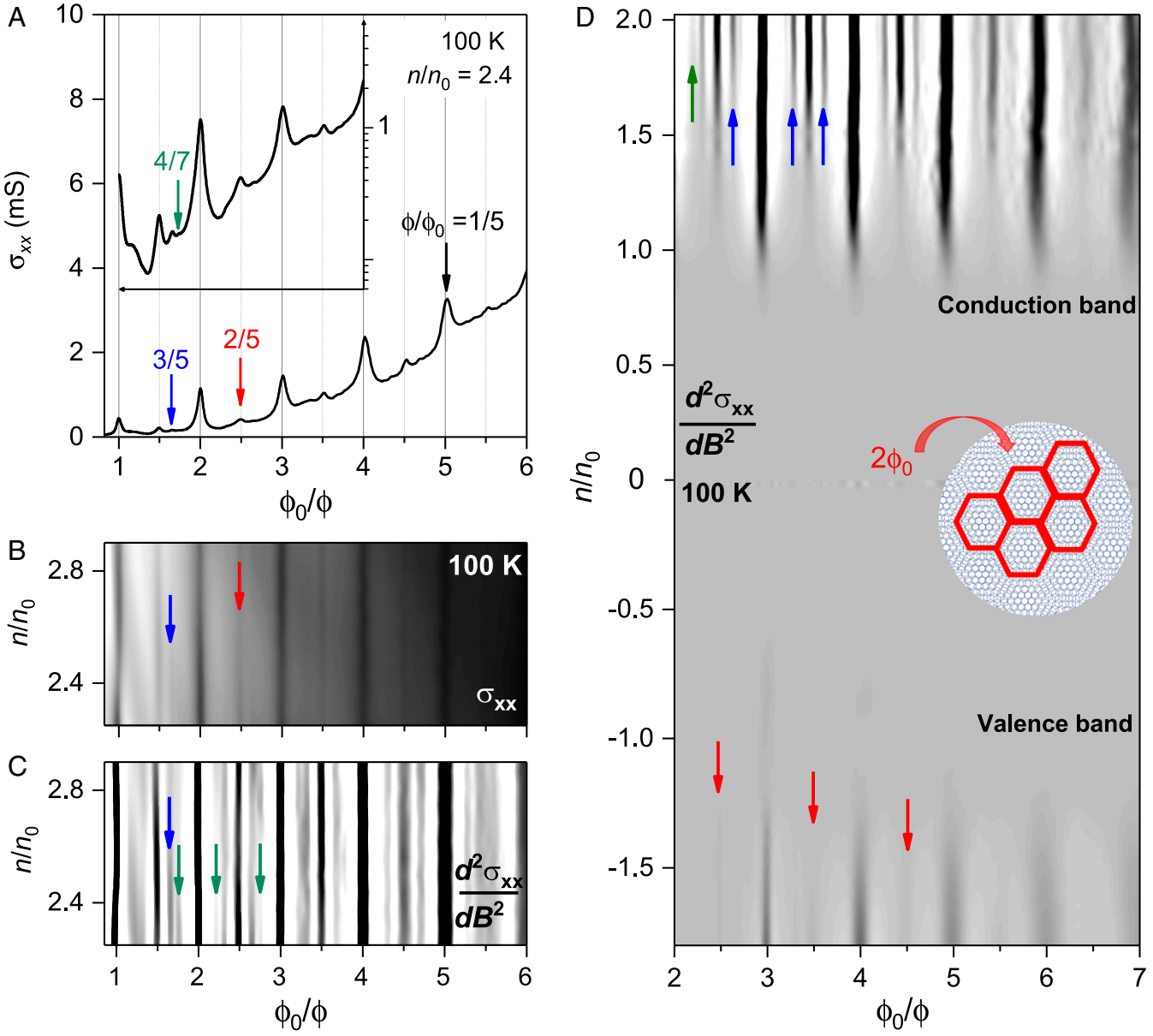

Fig. 2. High-order magnetic Bloch states. (*A*) σ_{xx} as a function of *B* expressed in units, ϕ_0/ϕ. (*Inset*) Same data on a logarithmic scale to emphasize weak features; the same horizontal axes. (*B*) $\sigma_{xx}(\phi_0/\phi,n)$ for high electron doping in *B* up to 30 T ($\phi > \phi_0$) where fractal features are most visible. Logarithmic gray scale: white 0.05 mS; black 5 mS. (*C*) Second derivative $d^2\sigma_{xx}/dB^2$ of the data in *B*. Gray scale: white 0 mS/T^2; black −0.05 mS/T^2. (*D*) Same as in *C* but using another data set obtained in *B* up to 15 T. The black, red, blue, and green arrows mark fractions with p = 1, 2, 3, and 4, respectively. The schematic in *D* illustrates the fractal state ϕ/ϕ_0 = 2/5, which involves an extended unit cell of five original moiré unit cells that share two flux quanta between them.

at unit fractions of $\phi/\phi_0 = 1/q$, in agreement with the previous report (21). In addition, several other maxima become clearly visible at fractions of $\phi/\phi_0 = 2/q$ and $3/q$. For high *B*, maxima at $\phi/\phi_0 = 4/q$ can also be discerned (Fig. 2 *A* and *C*, *Inset*).

To better visualize the additional maxima with $p > 1$, we exploit one of the defining features of BZ oscillations, namely that their frequency is independent of *n*. Fig. 2*B* plots a map of σ_{xx} (n, ϕ_0/ϕ), which reveals a set of dark vertical streaks. They can be seen more clearly if we plot the second derivative of σ_{xx} with respect to *B* (Fig. 2*C*). The differentiation procedure effectively removes the smooth background and highlights the extra features by sharpening local maxima. The vertical streaks indicate the extra features appearing at the same *B* for all *n*. Even the maxima for $p = 4$ become clearly distinguishable as faint gray features independent of *n* (green arrows in Fig. 2*C*). The observed behavior signifies that the additional maxima are caused by high-order magnetic Bloch states. Note that several $p = 2$ maxima can also be observed for hole doping (Fig. 2*D*), despite the poor visibility of BZ oscillations in graphene's valence band (21).

For certain ranges of *n* and *B*, we were able to identify all of the magnetic Bloch states up to a fourth order which can occur within the field interval $1/(q + 1) < \phi/\phi_0 < 1/q$. This is illustrated in Fig. 3 for $q = 2$. At 100 K (black curve), the hierarchy of magnetic Bloch states creates a fractal pattern in the magnetoconductivity, that is, the behavior of σ_{xx} close to zero applied magnetic field (Fig. 3, *Inset*) is replicated multiple times at increasingly smaller scales of *B*. As *T* increases, the fractions with large *p* become smeared and only those with $p = 1$ remain (Fig. 3).

To understand the observed hierarchy of states, let us first recall how the energy spectrum of graphene superlattices looks

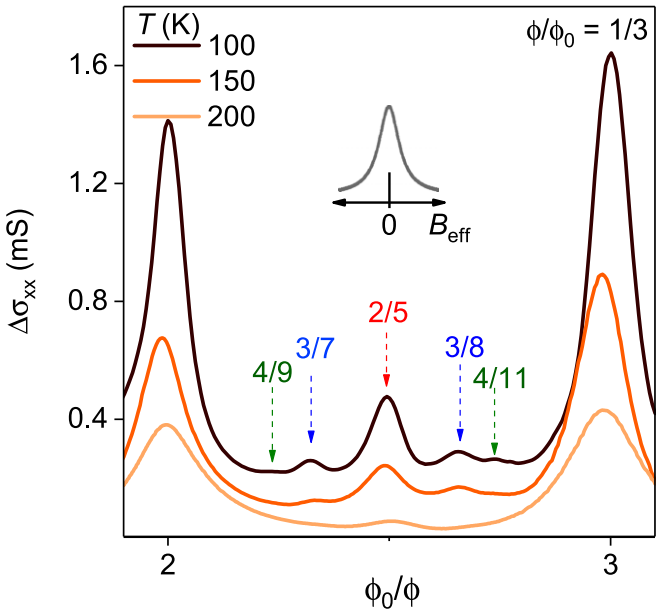

Fig. 3. Temperature dependence of high-order states. Longitudinal conductivity after subtracting a smooth background, $\Delta\sigma_{xx}$ (ϕ_0/ϕ). Three different T for $n = 2.2\ n_0$. The arrows indicate fields where the fractal magnetic Bloch states with $p = 2$, 3, and 4 are expected. The curves are shifted vertically for clarity. (*Inset*) Standard behavior of σ_{xx} (B) for metallic systems near zero magnetic field, either applied (B) or effective (B_{eff}). The shape is described by the classical expression $\sigma_{xx} \propto 1/[1 + (\mu B)^2]$, where μ is the charge carrier mobility (31, 32).

in quantizing magnetic fields (13, 37–39). Fig. 4*A* plots the computed density of states in the conduction band as a function of energy and B, producing an image often referred to as the Hofstadter butterfly (8) (*SI Appendix*, S3). In general, the spectrum is dominated by localized states which are caused by Landau quantization. They occur at irrational values of ϕ/ϕ_0 and appear as numerous discontinuous regions marked by black dots. However, at rational $\phi/\phi_0 = p/q$ the spectrum becomes continuous due to the emergence of magnetic Bloch states (6, 7). These are represented by solid vertical lines in Fig. 4*A* and appear each time when p flux quanta pierce a so-called supercell that has an area q times larger than the moiré unit. For example, a magnetic Bloch state at $\phi/\phi_0 = 2/5$ (red line in Fig. 4*A*) arises if two flux quanta penetrate through a supercell that is five times larger than the moiré unit cell (Fig. 2*D*, *Inset*). We also note that, for $n < n_0$, the superlattice spectrum is gapped over a wide range of B. This behavior is specific to Dirac electrons (37–39) and explains why BZ oscillations and high-order maxima in σ_{xx} are absent at low n (Fig. 2*D*).

The visibility of a particular magnetic Bloch state is determined by both the number of flux quanta (p) and the number of unit cells (q) associated with the state. As q increases, its visibility is expected to decrease because the Bloch state involves an increasingly larger supercell that might not be fully traversable by electrons because of their limited mean-free path. This explains why first-order states that follow the sequence $\phi/\phi_0 = 1/q$ (that is, BZ oscillations) tend to be more prominent (Fig. 1 *D* and *E*). Note that this tendency does not always hold (see Fig. 2*A* for ϕ/ϕ_0 approaching unity and the discussion below). As for the p dependence, its details are more subtle. When the supercell size is fixed by q, the maxima in σ_{xx} still become progressively smaller with increasing p. This is evident from the sequence $\phi/\phi_0 = p/5$ shown in Fig. 2*A* (highlighted by the colored arrows). To understand the p dependence, we recall (30–32) that transport of Bloch electrons also depends on their group velocity (v) as $\sigma_{xx} \propto v^2\tau$, where τ is the scattering time. Assuming that τ is independent of B (32), maxima in σ_{xx} should be determined by the value of v, which reflects the width of the energy bands of the

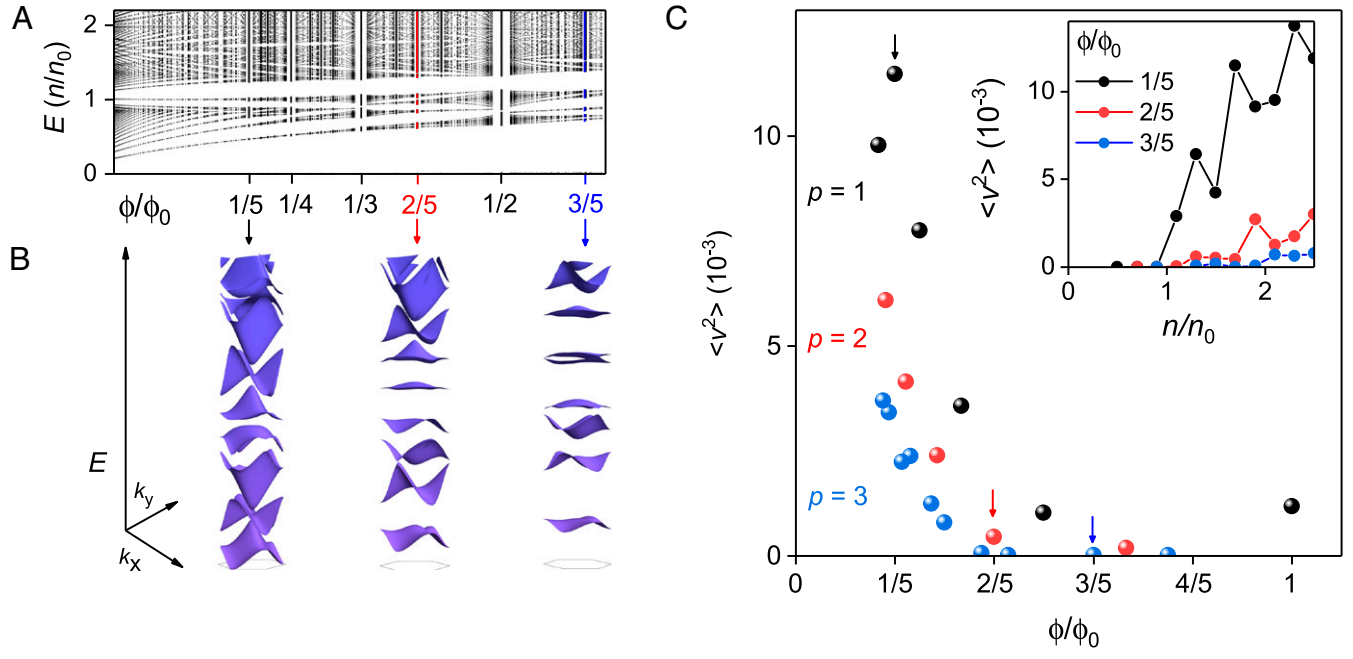

Fig. 4. Computed hierarchy of magnetic Bloch states. (*A*) A part of the Hofstadter butterfly for electrons in graphene/hBN superlattices (21, 39). The black and white regions signify allowed states and energy gaps, respectively. The red and blue vertical lines highlight the Bloch states at $\phi/\phi_0 = 2/5$ and 3/5, respectively. Note that the white vertical stripes around $\phi/\phi_0 = p/q$ indicate regions omitted in the calculations for technical reasons (too-dense spectrum) (21, 39). (*B*) Energy dispersions for the Bloch states with $\phi/\phi_0 = 1/5$, 2/5, and 3/5 over an energy interval from 0.2 to 0.3 eV, which approximately reflects the doping level in our measurements. (*C*) Average group velocity $\langle v^2\rangle$ for $n/n_0 = 1.7$. The values are normalized by graphene's Fermi velocity. Fractal states with different p are color-coded. The black, red, and blue arrows indicate the 1/5, 2/5, and 3/5 states shown in *B*. (*Inset*) $\langle v^2\rangle$ as a function of n/n_0 for those three states.

corresponding states. Broad bands imply higher electron velocities than flat bands (31). With this in mind, Fig. 4*B* shows the energy dispersion for the magnetic Bloch states at $\phi/\phi_0 = 1/5$, 2/5, and 3/5 (same q but different p). In general, the minibands contain many closely spaced subbands that either overlap or are separated by small gaps. As p increases, the minibands become flatter and the gaps separating them more pronounced. This suggests that v is smaller for magnetic Bloch states with larger p.

For further analysis, we calculated the group velocity for different magnetic Bloch states and, to account for the relatively high T of our measurements, took an average over the interval of thermal smearing (*SI Appendix*, S4). Fig. 4*C* plots the resulting mean-square velocity $\langle v^2 \rangle$ as a function of rational ϕ/ϕ_0 at a fixed n for $p = 1$, 2, and 3 and various q. Clearly, the states with larger p have a systematically smaller v. For example, the average velocity for $\phi/\phi_0 = 2/5$ is 10 times smaller than that for $\phi/\phi_0 = 1/5$. This proves that magnetic Bloch states with flatter bands exhibit lower average v and, therefore, lower σ_{xx}. The latter makes it harder to resolve the states experimentally and explains the observed p dependence of the local maxima in Figs. 2 and 3. We note that the calculated $\langle v^2 \rangle$ shows the same trend with p for hole doping in the valence band (*SI Appendix*, S5). Furthermore, at small q, local maxima in σ_{xx} become dependent not only on the supercell size (defined by q) but also on details of the miniband structure, that is, on $\langle v^2 \rangle$. For example, the nonmonotonic dependence of the first-order peaks in Fig. 2*A* ($\phi/\phi_0 = 1/q$) can be attributed to the interplay between the supercell size and $\langle v^2 \rangle$. Although magnetic Bloch states are formed more easily at small q (high B), their average speed becomes significantly smaller (Fig. 4*C*), which reduces the local maxima in σ_{xx}.

Finally, we consider the n dependence of high-order fractal states. Fig. 4*C* (*Inset*) plots $\langle v^2 \rangle$ as a function of n/n_0 for the minibands shown in Fig. 4*B* ($\phi/\phi_0 = p/5$). For all of the fractions, $\langle v^2 \rangle$ increases with n, in agreement with our experiment that shows more prominent fractal features at higher doping. The origin of higher $\langle v^2 \rangle$ in this case stems from the fact that the minibands become closely spaced at higher energies (Fig. 4 *A* and *B*). Accordingly, the Fermi level becomes smeared over an increasing number of minibands, which in turn increases σ_{xx} and, therefore, the visibility of magnetic Bloch states at high n. Note that some of the minibands are likely to have nonzero Chern numbers that can result in nonzero Hall conductivity in zero B_{eff} and, at low T, in chiral edge states (33, 34). However, the topological properties should not affect the discussed dissipative σ_{xx} in the linear response to the current-driving electric field.

To conclude, in addition to BZ oscillations that are periodic in $1/B$ and correspond to $\phi = \phi_0/q$, magnetotransport in graphene superlattices exhibits a fractal pattern due to high-order magnetic Bloch states that are in principle expected for all rational $\phi/\phi_0 = p/q$ and are clearly observed in our experiments for $p = 2$, 3, and 4. These high-order states require sufficiently high electron doping to become visible experimentally, and their hierarchy is associated with increasingly flatter Bloch minibands at higher p. Further work is required to understand the effect of topology and nonzero Chern numbers associated with magnetic minibands (39) on transport properties of graphene superlattices.

ACKNOWLEDGMENTS. This work was supported by Engineering and Physical Sciences Research Council (EPSRC), the European Graphene Flagship, the Royal Society, the Lloyd's Register Foundation, the European Research Council (ERC), and the Netherlands Organisation for Scientific Research. A.M. acknowledges the support from the EPSRC Early Career Fellowship EP/N007131/1. R.K.K. was supported by EPSRC Doctoral Prize Fellowship EP/N509565/1. U.Z. and S.P. acknowledge the support of High Field Magnet Laboratory–Radboud University, member of the European Magnetic Field Laboratory. G.H.A. acknowledges support from the EPSRC under Grant EP/M507969/1. L.A.P. acknowledges the Royal Society under Grant UF120297. V.I.F. was supported by EPSRC (EP/N010345), the ERC Synergy Grant Hetero 2D (ERC-2012-SyG), and the European Graphene Flagship (H2020-SGA-FET-GRAPHENE-2017). R.K.K., G.H.A., and V.I.F. acknowledge support from the Graphene NOWNANO Doctoral Training Centre.

1. Bloch F (1929) Über die Quantenmechanik der Elektronen in Kristallgittern. *Z Phys* 52:555–600.
2. Landau LD (1930) Diamagnetismus der Metalle. *Eur Phys J* 64:629–637.
3. Peierls R (1933) On the theory of diamagnetism of conduction electrons. *Z Phys* 80:763–791.
4. Wannier GH, Fredkin DR (1962) Decoupling of Bloch bands in the presence of homogeneous fields. *Phys Rev* 125:1910–1915.
5. Harper PG (1955) The general motion of conduction electrons in a uniform magnetic field, with application to the diamagnetism of metals. *Proc Phys Soc A* 68:879–892.
6. Brown E (1964) Bloch electrons in a uniform magnetic field. *Phys Rev* 133:A1038–A1044.
7. Zak J (1964) Magnetic translation group. *Phys Rev* 134:A1602–A1606.
8. Hofstadter DR (1976) Energy levels and wave functions of Bloch electrons in rational and irrational magnetic fields. *Phys Rev B* 14:2239–2249.
9. Xue J, et al. (2011) Scanning tunnelling microscopy and spectroscopy of ultra-flat graphene on hexagonal boron nitride. *Nat Mater* 10:282–285.
10. Decker R, et al. (2011) Local electronic properties of graphene on a BN substrate via scanning tunneling microscopy. *Nano Lett* 11:2291–2295.
11. Yankowitz M, et al. (2012) Emergence of superlattice Dirac points in graphene on hexagonal boron nitride. *Nat Phys* 8:382–386.
12. Yang W, et al. (2013) Epitaxial growth of single-domain graphene on hexagonal boron nitride. *Nat Mater* 12:792–797.
13. Ponomarenko LA, et al. (2013) Cloning of Dirac fermions in graphene superlattices. *Nature* 497:594–597.
14. Dean CR, et al. (2013) Hofstadter's butterfly and the fractal quantum Hall effect in moiré superlattices. *Nature* 497:598–602.
15. Hunt B, et al. (2013) Massive Dirac fermions and Hofstadter butterfly in a van der Waals heterostructure. *Science* 340:1427–1430.
16. Yu GL, et al. (2014) Hierarchy of Hofstadter states and replica quantum Hall ferromagnetism in graphene superlattices. *Nat Phys* 10:525–529.
17. Wang L, et al. (2015) Evidence for a fractional fractal quantum Hall effect in graphene superlattices. *Science* 350:1231–1234.
18. Yang W, et al. (2016) Hofstadter butterfly and many-body effects in epitaxial graphene superlattice. *Nano Lett* 16:2387–2392.
19. Wannier GH (1978) A result not dependent on rationality for Bloch electrons in a magnetic field. *Phys Status Solidi B Basic Res* 88:757–765.
20. Schubnikow L, De Haas WJ (1930) A new phenomenon in the change of resistance in a magnetic field of single crystals of bismuth. *Nature* 126:500.
21. Krishna Kumar R, et al. (2017) High-temperature quantum oscillations caused by recurring Bloch states in graphene superlattices. *Science* 357:181–184.
22. Kretinin AV, et al. (2014) Electronic properties of graphene encapsulated with different two-dimensional atomic crystals. *Nano Lett* 14:3270–3276.
23. Woods CR, et al. (2014) Commensurate–Incommensurate transition in graphene on hexagonal boron nitride. *Nat Phys* 10:451.
24. Mayorov AS, et al. (2011) Micrometer-scale ballistic transport in encapsulated graphene at room temperature. *Nano Lett* 11:2396–2399.
25. Wang L, et al. (2013) One-dimensional electrical contact to a two-dimensional material. *Science* 342:614–617.
26. Ben Shalom M, et al. (2015) Quantum oscillations of the critical current and high-field superconducting proximity in ballistic graphene. *Nat Phys* 12:318.
27. Wallbank JR, Patel AA, Mucha-Kruczyński M, Geim AK, Fal'ko VI (2013) Generic miniband structure of graphene on a hexagonal substrate. *Phys Rev B* 87:245408.
28. Wang E, et al. (2016) Gaps induced by inversion symmetry breaking and second-generation Dirac cones in graphene/hexagonal boron nitride. *Nat Phys* 12:1111–1115.
29. Ju L, et al. (2014) Photoinduced doping in heterostructures of graphene and boron nitride. *Nat Nanotechnol* 9:348–352.
30. Ashcroft N, Mermin ND (1976) *Solid State Physics* (Holt, Rinehart and Winston, New York).
31. Soloym J (2003) *Fundamentals of the Physics of Solids*, Electronic Properties (Springer, Berlin), Vol 2.
32. Beenakker CWJ, van Houten H (1991) Quantum transport in semiconductor nanostructures. *Semiconductor Heterostructures and Nanostructures*, eds Ehrenreich H, Turnbull D (Academic, Boston), Vol 44, pp 1–228.
33. Thouless DJ, Kohmoto M, Nightingale MP, den Nijs M (1982) Quantized Hall conductance in a two-dimensional periodic potential. *Phys Rev Lett* 49:405–408.
34. Streda P (1982) Quantised Hall effect in a two-dimensional periodic potential. *J Phys C Solid State Phys* 15:L1299.
35. Haldane FDM (1988) Model for a quantum Hall effect without Landau levels: Condensed-matter realization of the "parity anomaly". *Phys Rev Lett* 61:2015–2018.
36. Spanton EM, et al. (2018) Observation of fractional Chern insulators in a van der Waals heterostructure. *Science* 360:62–66.
37. Diez M, Dahlhaus JP, Wimmer M, Beenakker CWJ (2014) Emergence of massless Dirac fermions in graphene's Hofstadter butterfly at switches of the quantum Hall phase connectivity. *Phys Rev Lett* 112:196602.
38. Moon P, Koshino M (2014) Electronic properties of graphene/hexagonal-boron-nitride moire superlattice. *Phys Rev B* 90:155406.
39. Chen X, et al. (2014) Dirac edges of fractal magnetic minibands in graphene with hexagonal moiré superlattices. *Phys Rev B* 89:75401.